Physica B: Condensed Matter 560 (2019) 228–235

Contents lists available at ScienceDirect

Physica B: Condensed Matter

journal homepage: www.elsevier.com/locate/physb

Study of mixed-valence Mn_2BO_4 using XRD, XPS and XAFS spectroscopies

N.V. Kazak[a,*], M.S. Platunov[a], Yu.V. Knyazev[a], E.M. Moshkina[a], L.A. Solovyov[b], S.N. Vereshchagin[b], Yu.L. Mikhlin[b], A.A. Veligzhanin[c], A.L. Trigub[c], S.G. Ovchinnikov[a]

[a] Kirensky Institute of Physics, Federal Research Center KSC SB RAS, 660036, Krasnoyarsk, Russia
[b] Institute of Chemistry and Chemical Technology, Federal Research Center KSC SB RAS, 660036, Krasnoyarsk, Russia
[c] National Research Centre "Kurchatov Institute", 123182, Moscow, Russia

ARTICLE INFO

Keywords:
Charge-ordering
Mixed-valence
XAS
XRD
XPS

ABSTRACT

The valence states and local structure around Mn atoms in mixed-valence Mn_2BO_4 have been studied by temperature dependent X-ray powder diffraction (XRPD), X-ray photoelectron (XPS) and Mn *K*-edge X-ray absorption (XAFS) spectroscopies measurements. X-ray absorption near-edge structure (XANES) and XPS have been used to measure the average oxidation state of Mn in bulk and near-surface of the material. The edge position, peak shapes and pre-edge features of Mn *K*-edge XANES spectra have been discussed. The pronounced temperature dependence of the Debye-Waller (DW) factor corresponding to the Mn—O coordination shell has been found from the extended x-ray absorption fine structure (EXAFS) analysis and has been associated with variations in the local distortions in MnO_6 octahedra and emergence of short-range magnetic correlations at low temperatures. The XRPD measurements have been carried out at 298, 523 and 773 K. The monoclinic symmetry ($P2_1/n$) was found to persist up to highest temperature measured. The BVS calculations have revealed large valence difference between two manganese sites that strongly supports the presence of charge ordering up to high temperatures.

1. Introduction

It is known that the charge ordering (CO) phenomenon plays an important role in magnetic and transport properties of 3*d*-oxides leading to the colossal magnetoresistance in manganites [1] and the Verwey transition in magnetite [2]. Warwickites with general formula $M^{2+}M^{3+}BO_4$ are rare materials where one element can adopt different oxidation states and therefore the conditions for order-disorder CO transition exist. Moreover, the warwickites are of interest due to the quasi low-dimensionality, quantum entanglement, structural and electronic transitions [3–7]. The basic crystal structure is usually described by orthorhombic (*Pnma*). A unit cell contains 4 formula units and two crystallographically non-equivalent metal sites that are labeled as 1 and 2 (Fig. 1). The metal ions are surrounded by oxygen octahedra. The octahedra are linked by edge sharing so as four octahedra form flat ribbons extending along the *c*-axis. A heterometallic warwickites ($M^{2+} \neq M^{3+}$ = Mg, Mn, Co, Ni, Cr, Ti, V, Fe, Sc, *etc.*) are naturally disordered systems showing a spin-glass behavior [8–15]. The spin-glass transition T_{SG} occurring at a relatively low temperature is a result of the emergence of exchange interaction between the low-dimensional ribbons.

Up to now, only two homometallic warwickites Fe_2BO_4 and Mn_2BO_4 which exhibit quite different magnetic and electronic properties have been known [16,17]. Recently, a vanadium mixed-valence warwickite V_2BO_4 has been synthesized [18]. The Fe_2BO_4 shows both commensurately and incommensurately modulated charge ordered phases at low temperatures ($T_{CO} < 340$ K) and the valence fluctuating state (due to a Fe^{2+} - Fe^{3+} electron hopping) above T_{CO}. Different techniques have been applied to investigate the charge distribution in Fe_2BO_4: Mössbauer spectroscopy, resonant X-ray diffraction, transmission electron microscopy, and electronic structure calculations [19–22]. High pressure Mössbauer spectroscopy (MS) study has shown a strong interplay between CO and magnetism, with an electronic phase transition boundary at $P \approx 16$ GPa [23]. Fe_2BO_4 is an *L*-type ferrimagnet with $T_C = 155$ K and a semiconductor with a conductivity activation energy $E_a = 0.37$ eV [7,24]. In total contrast, Mn_2BO_4 is an antiferromagnet with a relatively low transition temperature $T_N = 26$ K and an insulator [25,26]. Charge ordering in this compound has been less investigated experimentally through the empirical bond-valence-sum analysis (BVS) and theoretically using the high-spin filling (hsf) scheme in the extended Hückel approach [27]. The atomic charges for Mn1 and Mn2 sites at room temperature have been found equal to 2.95 and 2.01,

* Corresponding author.
E-mail address: nat@iph.krasn.ru (N.V. Kazak).

https://doi.org/10.1016/j.physb.2019.02.019
Received 5 October 2018; Received in revised form 11 February 2019; Accepted 12 February 2019
Available online 15 February 2019
0921-4526/

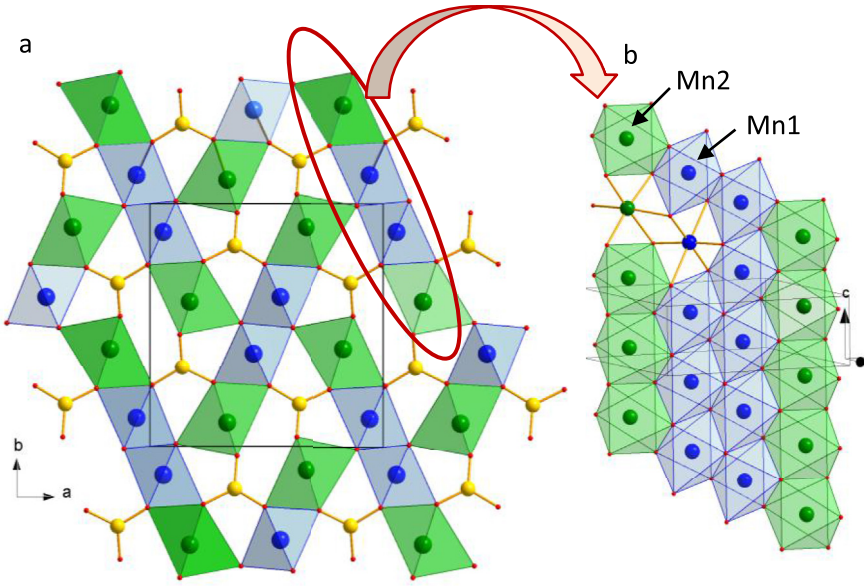

Fig. 1. a) Crystal structure of Mn_2BO_4 projected in the *ab*-plane.The blue and green spheres at the centers of the octahedra denote two crystallographic nonequivalents Mn positions. The small yellow spheres denote B atoms. b) A ribbons composed of edge-shared MnO_6 octahedra are propagated along the *c*-axis. (For interpretation of the references to color in this figure legend, the reader is referred to the Web version of this article.)

respectively. The charge ordering has been found to be associated with the orbital ordering in the presence of a x^2-y^2 hole localized at Mn^{3+}, while in Fe_2BO_4, the charge ordering is related to the electron-electron coupling.

Recent high resolution synchrotron powder X-ray diffraction experiment on the homometallic vanadium warwickite V_2BO_4 which is adopt orthorhombic crystal structure (*Pnma*) at room temperature has shown the change of the crystallographic symmetry upon cooling that was assigned to emergence of a complex charge ordering [18].

With this respect, a direct probe of charge states and their evolution with temperature becomes critical for fundamental understanding physical properties of these oxyborates. Herewith, we apply a bulk (XANES) and near-surface (XPS) techniques to study the manganese oxidation states in mixed-valence warwickite Mn_2BO_4. The photoelectron spectra (Mn 2*p* and others) have been studied at room temperature. Mn *K*-edge XANES spectra have been measured from 8.8 to 500 K. The calibration method which correlates the oxidation state to the energy position of major features in XANES spectra of deliberately selected reference compounds has been used. Both Mn^{2+} and Mn^{3+} ions are shown to be present in the compound with the average oxidation state of (2.55 ± 0.08)+ which is very close to nominal 2.50+ determined by the stoichiometry. The analysis of structural parameters and BVS calculations clearly show that the oxidation states of Mn^{2+} and Mn^{3+} can be assigned to the different Mn sites supporting the retention of charge ordering at high temperatures.

2. Experimental techniques

Needle-shaped single crystalline specimens of Mn_2BO_4 have been synthesized using a flux method in the system $Bi_2Mo_3O_{12}$ - B_2O_3 – Mn_2O_3 – Na_2CO_3 [26].

The X-ray powder diffraction investigations were carried out on a PANalyticalX'Pert PRO diffractometer equipped with a solid-state detector PIXcel and a graphite monochromator at Cu Kα radiation. The crystal structure was refined using the Rietveld method [28] with the full-profile derivative difference minimization (DDM) [29] at 298, 523 and 773 K. The high-temperature measurements were performed up to 973 K with an Anton Paar HTK1200 stage.

X-ray photoelectron spectra from crystals crushed immediately before the experiment and attached to sticky carbon tape were measured with a SPECS instrument equipped with a PHOIBOS 150 MCD 9 hemispherical analyzer at electron take-off angle 90° with the pass energy of 8 eV for high-resolution spectra and 20 eV for survey spectra. The pressure in an analytical chamber was in the range of 10^{-9} mBar. The spectra were excited by Mg Kα irradiation (1253.6 eV) of an X-ray tube. Flood electron gun was used to eliminate heterogeneous electrostatic charging of the material. The high-resolution spectra were fitted with Gaussian-Lorentzian peak profiles after subtraction of a Shirley-type background using a CasaXPS software package.

X-ray absorption near-edge structure (XANES) and extended X-ray absorption fine structure (EXAFS) spectra at the Mn *K*-edge were recorded at temperatures ranging from 8.8 K to 500 K in the transmission mode using a SHI closed-cycle helium refrigerator (Japan) at the Structural Materials Science beamline (National Research Center "Kurchatov Institute", Moscow). The storage ring operated at an electron energy of 2.5 GeV and an average electron current of about 80 mA. For the selection of the primary beam photon energy, a Si (111) channel-cut monochromator was employed, which provided an energy resolution $\Delta E/E \sim 2{\cdot}10^{-4}$. Primary and transmitted intensities were recorded using two independent ionization chambers filled with appropriate N_2/Ar mixtures providing 20% and 80% absorption, respectively. The energy was calibrated against a sharp Mn *K*-edge pre-edge feature of $KMnO_4$. The EXAFS spectra were collected using optimized scan parameters of the beamline software. The ΔE scanning step in the XANES region was about 0.4 eV, and scanning in the EXAFS region was carried out at a constant step on the photoelectron wave number scale with $k = 0.05 Å^{-1}$, giving energy step of the order of 1.5 eV. Single-crystalline samples were ground to fine powders and then spread uniformly onto a thin adhesive Kapton film and folded into several layers to give an absorption edge jump around unity.

The EXAFS spectra $\mu(E)$ were normalized to an edge jump and the absorption coefficient of the isolated atoms $\mu_0(E)$ was extracted by fitting a cubic-spline-function to the data. After subtraction of the smooth atomic background, the conversion from E to k scale was performed. Crystallographic structural parameters were used as starting model. The k^3-weighted EXAFS function $\chi(k)$ was calculated in the intervals $k = 2–12 Å^{-1}$ using a Hanning window (local order peaks were clearly distinguishable against background up to 7 Å). The EXAFS structural analysis was performed using theoretical phases and amplitudes as calculated by the FEFF-8 package [30], and fits to the experimental data were carried out in the *R*-space with the IFEFFIT package [31].

The thermal behavior of Mn_2BO_4 sample was studied using a simultaneous TG-DSC apparatus STA 449C Jupiter equipped with an

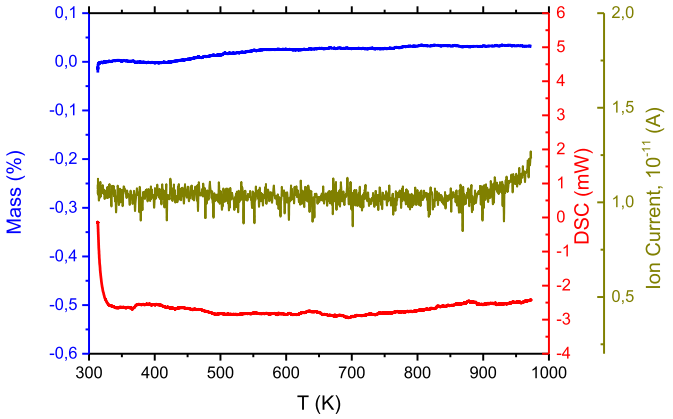

Fig. 2. TG (blue), DSC (red) curves and ion current of $m/z = 32$ (O_2^+) as a function of temperature. Argon flow, β = 10 K/min. (For interpretation of the references to color in this figure legend, the reader is referred to the Web version of this article.)

Aëolos QMS 403C mass spectrometer (NETZSCH, Germany) under dynamic argon flow (~0.005% O_2) in Pt crucibles, ramp rate 10 K/min. The TG/DSC investigation has not revealed a detectable change in the weight of the sample when heated from 313 to 900 K. Under these conditions, no oxygen evolution has been detected according to the monitoring the composition of the gas phase by an on-line mass spectrometer (Fig. 2).

3. Results and discussion

3.1. High-temperature XRPD

In the whole temperature range studied ($298 \le T(K) \le 773$), the XRPD patterns were refined in a monoclinic symmetry ($P2_1/n$) (Fig. 3). The structural parameters, atomic coordinates, representative interatomic distances, and isotropic displacement parameters, are given in Tables 1–4 of Supplementary materials [32]. No secondary manganese-contained phases have been detected by means of X-ray diffraction. The room temperature parameters are consistent with the data available in the literature [17,25,26]. The absence of structural phase transitions in the temperature interval studied is consistent with the high-temperature heat capacity data [33].

As for the coordination environments of the manganese ions, one can distinguish two types of distorted MnO_6 octahedra, displaying quite different sets of Mn−O distances (Table 1). Following the procedure proposed in Ref. [26] the main component of electrical field gradient (EFG) tensor V_{zz} has been calculated. The different signs of V_{zz} parameters indicate different tetragonal distortions for two sites. The Mn1 site has the biggest V_{zz} showing that this is the most distorted octahedron. As the temperature increases, the V_{zz} parameters increase reflecting the growth of the local distortions at both octahedra.

To assign the oxidation states to each manganese atom position the bond valences sums (BVS) calculation has been done [34]. Examination of the Mn_2BO_4 prepared in this study reveals the obvious propensity of manganese atoms to occupy different octahedral sites (the BVS values shown in bold in Table 1). The differences between the bond valence sums observed for the two sites are large as ΔBVS ≈1.0 valence unit (v.u.). In addition, the Mn1 octahedral site with the higher calculated BVS has much larger axial/equatorial bond length ratios than the Mn2 octahedral site with “lower BVS”. These observations are consistent with the presence of “small” (⟨Mn1−O⟩ ≈ 2.06 Å) Jahn-Teller distorted Mn^{3+} centers ordered with “large” (⟨Mn2−O⟩ ≈ 2.22 Å) less distorted Mn^{2+} centers and thus support the presence of charge ordering up to highest measured temperature. The fact that both Fe_2BO_4 and Mn_2BO_4 homometallic warwickites that adopt the monoclinic structure ($P2_1/c$ and $P2_1/n$, respectively) are charge ordered strongly suggests that this structure is the preferred when charge ordering is sufficiently energetically advantageous. The stabilization of the monoclinic structure by the charge ordering is derived from the stacking of the ordered octahedral chains. For Fe_2BO_4 a monoclinic twinning with similar weight of domains with opposite sings of monoclinic distortion was observed from XRD study and the sp.gr. *Pc* was found to arise from averaging domains with different diagonal order [19]. In Mn_2BO_4 the extended axial Mn−O bond lengths associated with the Jahn-Teller distortion of Mn1 site are stacked in double-chains manner leading to the ordering of strains. Such chain stacking is apparently compatible with the long-range charge order. The double chains of Mn^{3+} ions surrounded by the Mn^{2+} chains and $(BO_3)^{3-}$ tunnel anions form an equally spaced lattice. From an electrostatic point of view, there is a large gain in the energy if all Mn^{3+} ions stay at the most preferable sites. In other words, there is a periodicity of charge distribution, which is imposed by the lattice. Once such a long-range charge order occurs, the Mn^{3+} lattice is strongly pinned on a crystal lattice, resulting in the poor conductivity. The electron-lattice effects are expected to be important for this system.

3.2. X-ray photoelectron spectroscopy

The XPS survey spectrum (Fig. 4) shows no significant presence of impurities, except for the adventitious contaminant carbon and bismuth (~1%); the latter was presented in the flux. The $O^{2-}(1s)$ and $B^{3+}(1s)$ bands with the binding energies of 530.8 eV and 190.9 eV, respectively, are in good agreement with the energies for lattice oxygen O_L and BO_3 group reported for other borates [35,36]. Fig. 5 shows a characteristic Mn $2p_{3/2,1/2}$ spectrum of mixed-valence Mn_2BO_4, the interpretation of which is not strightfoward since the Mn 2*p* peaks are broad due to multiple splitting.

In order to elucidate the relative concentrations of Mn^{2+} and Mn^{3+}, the Mn $2p_{3/2}$ band was fitted (after subtraction of the Shirley-type background) using two sets of multiplet lines and the peak parameters for MnO and Mn_2O_3 oxides proposed by *Biesinger* et al. [37] (Table 2). In the fit, the binding energies and full widths at half maximum (FWHM) of the components were allowed to vary in the narrow ranges of ± 0.1 eV and ± 0.05 eV, respectively, and the relative intensities were fixed. The binding energies of the strongest Mn $2p_{3/2}$ peaks (641.2 and 642.1 eV) agree well with the values reported respectively for Mn^{2+} and Mn^{3+} [37,38], and the fractions of Mn^{2+} and Mn^{3+} were found to be 32.8% and 67.2%, respectively, yielding an average oxidation state 2.67+ that is somewhat larger than the ideal value of 2.50+. In particular, this may be due to oxidation of a share of surface Mn^{2+} upon the contact with atmosphere.

3.3. XANES/EXAFS

Fig. 6 shows the room-temperature normalized Mn *K*-edge XANES spectra of Mn_2BO_4. The $Mn_{1.3}Fe_{0.7}BO_4$ (where iron is trivalent ion [11]) and $Mn_{1.3}Mg_{0.7}BO_4$ oxyborates have been used as references for the $Mn^{2.22+}$ and $Mn^{2.78+}$ charge states in warwickite structure along with $MnBO_4$ and Mn_2O_3 oxides.

A weak pre-edge absorption feature at ~6536 eV originates from the $1s \rightarrow 3d$ transition, which is dipole forbidden, but quadrupole allowed. This transition gains some intensity due to non-centrosymmetric environments around Mn ions, *i.e.*, symmetry-violating distortions of the MnO_6 octahedra. A strong peak in the vicinity of ~6550 eV is assigned to a dipole-allowed transition $1s \rightarrow 4p$. The sample's absorption threshold lies between those of the reference compounds. The main feature is the step-like behavior of the absorption threshold near ~6546 eV that is better seen for Mn-Mg sample. Fig. 6(b) shows first derivatives of the respective experimental spectra. The derivatives demonstrate a doublet structure with components at ~6544 eV and ~6548 eV where the main maxim corresponds to the absorption edge of Mn. To obtain a quantitative estimate of the manganese oxidation

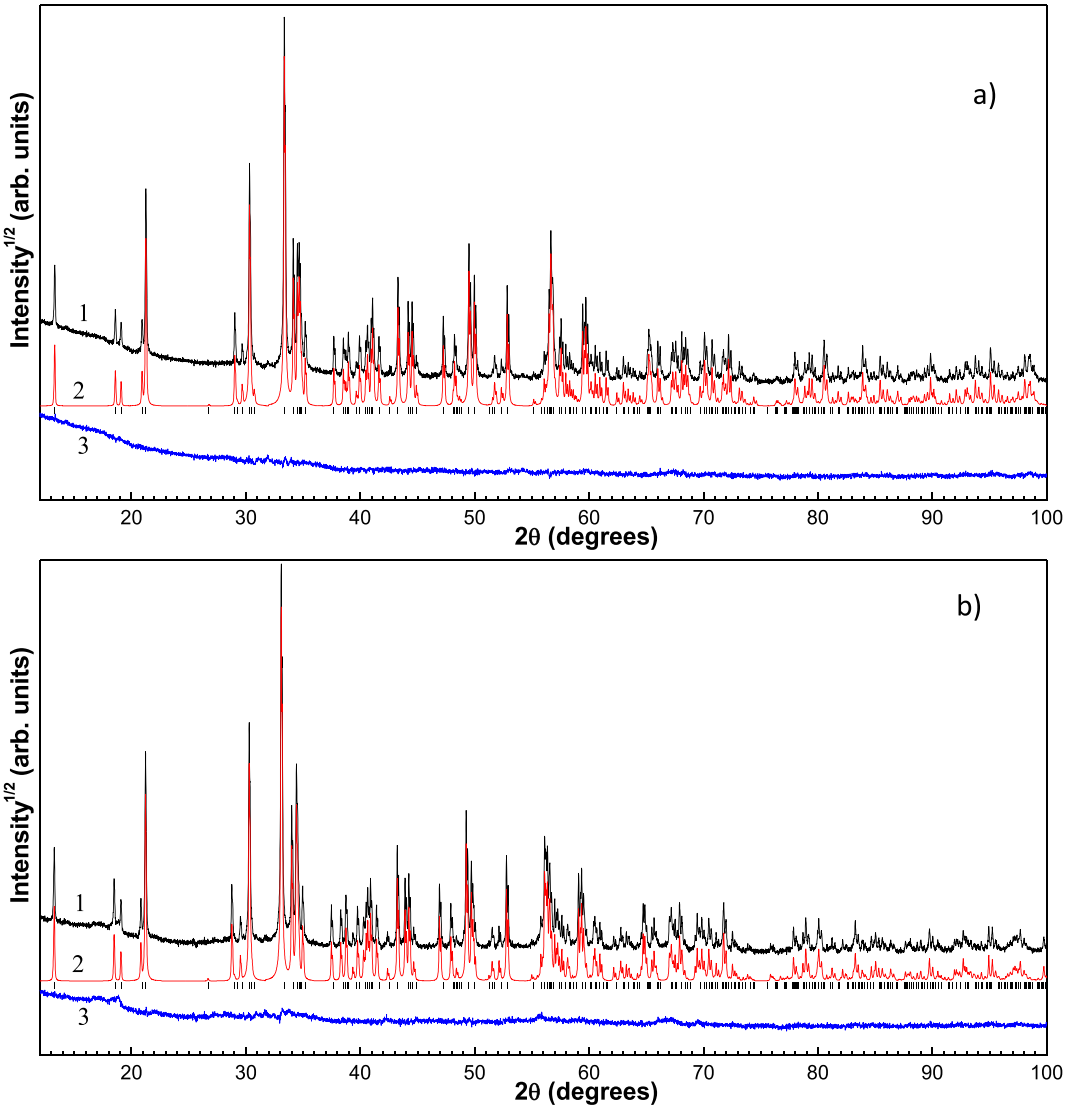

Fig. 3. Observed (1), calculated (2), and difference (3) XRPD patterns of Mn_2BO_4 at a) 298 K and b) 773 K after DDM refinement.

states, an *ad hoc* calibration procedure has been employed. Fig. 6(c) shows the Mn valence as a function of experimental Mn *K*-edge positions for reference compounds and for Mn_2BO_4. The dependence of the threshold energies versus the Mn oxidation state with the slope of ~0.50 ± 0.05 eV per oxidation number is seen. For Mn_2BO_4, the edge position corresponds to the Mn oxidation state of 2.55 ± 0.08. The evolution of experimental XANES spectra of Mn_2BO_4 over a wide temperature range is shown in Fig. 7. All spectra obtained from 8.8 to 300 K are similar to each other. No significant changes in the XANES spectra occur when passing through the magnetic ordering temperature

Table 1
The axial and equatorial Mn−O bond lengths for the octahedral sites Mn1 and Mn2; the ratio of the axial/equatorial bond lengths; the average metal-oxygen distances; the main component V_{zz} of EFG tensor; the charge state of metal ion determined by BVS method (the propensity of manganese atoms to occupy different sites is shown in bold); the bond valence sums difference.

T (K)		Mn−O *ax* (Å)	Mn−O *eq* (Å)	*ax/eq*	⟨Mn−O⟩ (Å)	V_{zz} (e/Å^3)	BVS[a] (v.u.)		ΔBVS (v.u.)
							Mn^{2+}	Mn^{3+}	
298	Mn1	2.324	1.927	1.206	2.059	−0.427	3.26 ± 0.02	**3.01** ± 0.02	1.05 ± 0.02
	Mn2	2.175	2.239	0.971	2.218	0.096	**1.96** ± 0.01	1.81 ± 0.01	
523	Mn1	2.344	1.929	1.215	2.068	−0.441	3.21 ± 0.02	**2.96** ± 0.02	1.02 ± 0.02
	Mn2	2.183	2.241	0.974	2.222	0.106	**1.94** ± 0.01	1.79 ± 0.01	
773	Mn1	2.355	1.936	1.216	2.076	−0.435	3.14 ± 0.02	**2.90** ± 0.01	0.97 ± 0.02
	Mn2	2.192	2.249	0.975	2.230	0.127	**1.93** ± 0.01	1.78 ± 0.01	

[a] The valence state of manganese ions for each of distinct site have been calculated using the bond valence sum $Z = \sum_i s_{ij}$ [34]. Here $s_{ij} = exp[(R_0 - r_{ij})/b]$ is the bond valence between *i* and *j* ions, R_0 is the parameter dependent on the nature of ions forming the *ij*-pair ($R_0(Mn^{2+}) = 1.790$ Å, $R_0(Mn^{3+}) = 1.760$ Å), $b = 0.37$ Å is the constant value, r_{ij} is the *ij*-pair bond length.

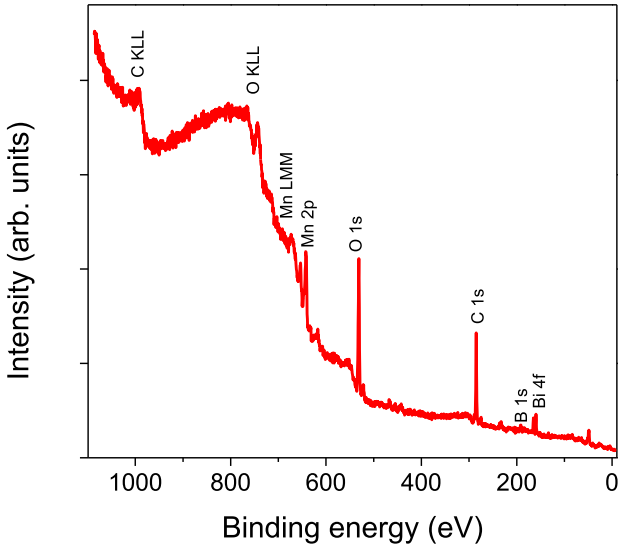

Fig. 4. XPS survey spectrum of Mn_2BO_4 crystals.

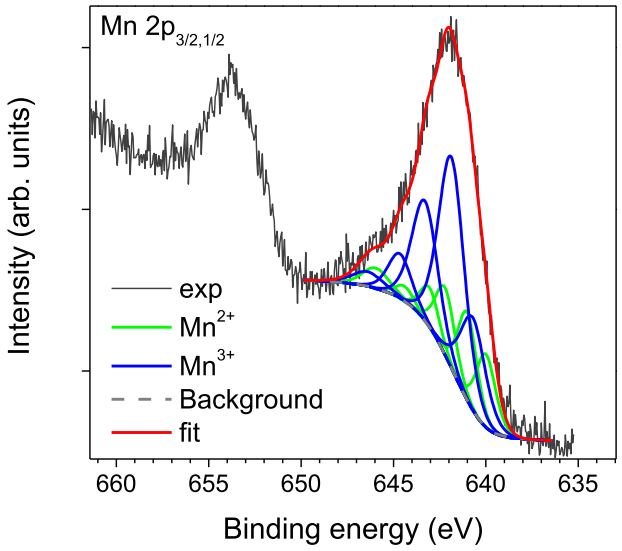

Fig. 5. XPS Mn2*p* spectra of Mn_2BO_4 crystals fitted for Mn^{2+} and Mn^{3+}.

Table 2
The fit parameters of main components of Mn 2*p* spectrum of Mn_2BO_4 single crystal: binding energies (± 0.1 eV), FWHM (± 0.05 eV), and total area A (%).

		P1	P2	P3	P4	P5	P6
Mn^{2+}	BE	640.0	641.0	642.20	643.05	644.39	645.95
	FWHM	1.25	1.20	1.25	1.20	1.20	1.69
	A (32.8)	7.8	9.1	7.3	4.2	1.5	2.9
Mn^{3+}	BE	640.70	641.86	643.30	644.66	646.55	–
	FWHM	1.60	1.65	1.65	1.5	1.99	–
	A (67.2)	12.6	29.7	16.9	5.6	2.4	–

T_N = 26 K, while a noticeable decrease in the intensity of the main peak at 6550 eV occurs in the high-temperature phase (T > 300 K). A slight change in the intensity of the first derivatives can be explained by a thermal broadening of the Fermi edge with temperature changes (inset Fig. 7) [39].

We have also studied temperature effects on the local structure distortion of the average MnO_6 octahedra through the EXAFS spectra analysis. Fig. 8 shows the Fourier transforms (FT) of the EXAFS functions at different temperatures. The features within 1–3 Å correspond to

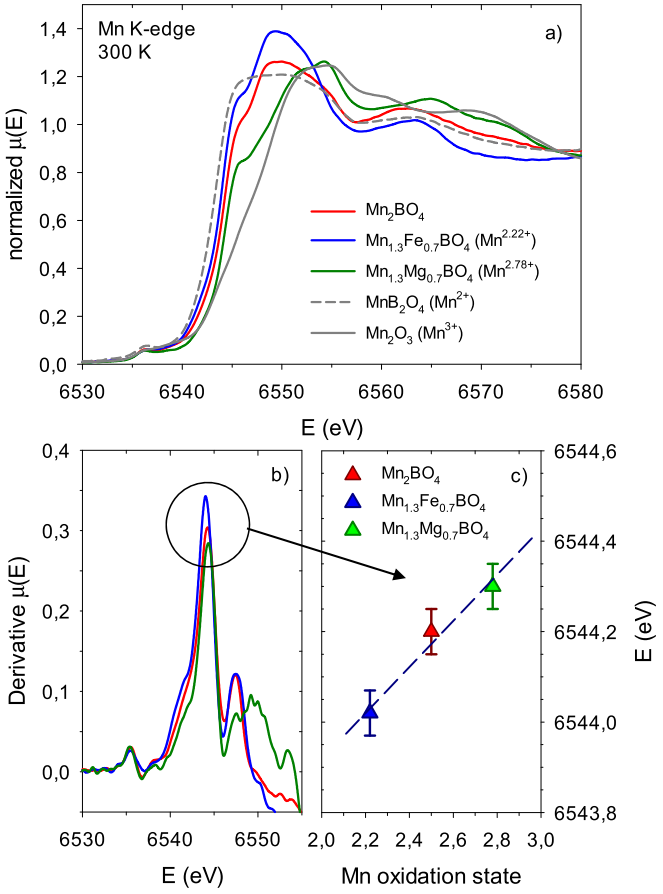

Fig. 6. a) Normalized Mn *K*-edge spectra of Mn_2BO_4 and reference manganese oxides with warwickite structure recorded at room temperature. b) The double structure of the first derivatives of warwickite's spectra (same colors). The shift of the main maximum at 6544 eV towards larger energies depends on the Mn oxidation state. c) Mn oxidation state versus experimental Mn *K*-edge position for reference warwickites and for Mn_2BO_4 sample. (For interpretation of the references to color in this figure legend, the reader is referred to the Web version of this article.)

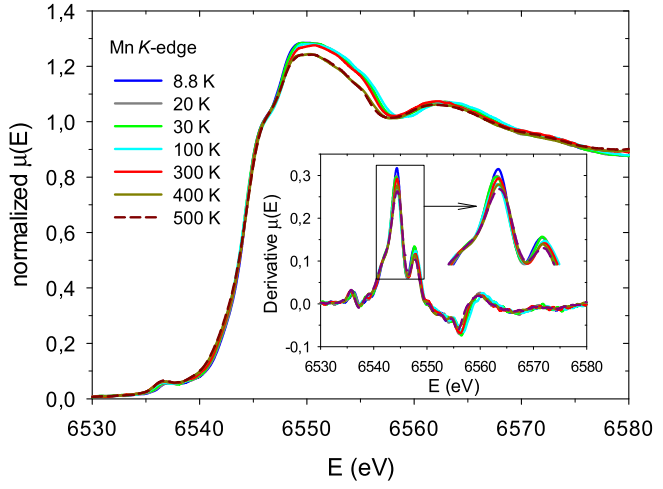

Fig. 7. Normalized Mn *K*-edge spectra of Mn_2BO_4 recorded in the range of 8.8–500 K. A noticeable decrease in the intensity of the main transition at T > 300 K is seen. The inset shows the first derivatives of Mn_2BO_4 spectra (same colors). The temperature-induced decrease in the intensity of the maxima is associated with a thermal broadening of Fermi edge. (For interpretation of the references to color in this figure legend, the reader is referred to the Web version of this article.)

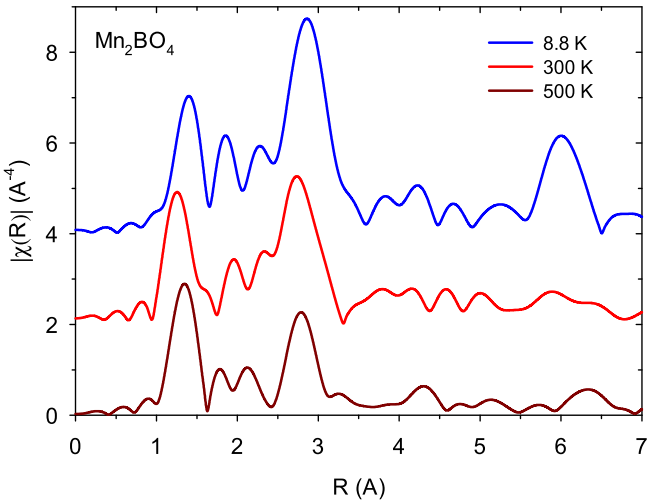

Fig. 8. FT modulus of the k^3-weighted EXAFS spectra of the Mn_2BO_4 warwickite at the Mn *K*-edge as a function of temperature. The curves have been vertically shifted for clarity.

the first oxygen coordination shell Mn—O and the nearest neighbors Mn–Mn within Mn—O—Mn chains. The contributions from higher-shell neighbors occur above 4 Å. The high intensity of the peak at ~6 Å, which is observed even at room temperature, points to the pronounced rigidity of chemical bonds that form this structure. The peak's intensities corresponding to the first and second coordination shells decrease as the temperature increases. The presence of two non-equivalent metal sites and low overall symmetry strongly complicate the quantitative EXAFS analysis. Therefore the discussion of EXAFS results was restricted to the first oxygen shell Mn—O. The interatomic distances $R_{Mn\text{-}O}$ and DW factor σ^2 were varied to achieve best fits. The fits at different temperatures were performed with a fixed value of the threshold energy shift $\Delta E_0 = 3$ eV obtained from the fit at the lowest temperature.

Fig. 9 compares the best-fit and experimental spectra in terms of FT moduli of k^3-weighted EXAFS signals and the real parts of back-Fourier-transformed spectra in *k*-space for $T = 8.8$ K. Similar agreements were obtained for all other temperatures. The room-temperature monoclinic crystallographic structure has been adopted to calculate theoretical amplitude and phases for each scattering path up to 7 Å. The first oxygen coordination shell can be reasonably simulated only using a set of five well separated Mn—O distances with the total coordination

Table 3
Best-fit structural parameters of the first oxygen coordination shell of the Mn_2BO_4 at the Mn *K*-edges. *N* is the coordination number, *R* is the inter-atomic distances for the octahedral site, σ^2 are the DW factors and R_f is the deviation factor of the $\chi_{theor}(k)$ from the $\chi_{exp}(k)$.

T (K)	Path	*N*	*R* (Å)	$\sigma^2 \cdot 10^{-3}$ (Å^2)	R_f (%)
8.8	Mn—O	1	1.90(2)	1.69(2)	1.918
		1	1.99(2)		
		2	2.15(2)		
		1	2.28(2)		
		1	2.38(2)		
	⟨Mn—O⟩		2.14(2)		
100		1	1.88(2)	2.94(2)	3.394
		1	1.96(2)		
		2	2.12(2)		
		1	2.26(2)		
		1	2.34(2)		
	⟨Mn—O⟩		2.11(2)		
300		1	1.88(2)	3.45(2)	4.678
		1	1.97(2)		
		2	2.13(2)		
		1	2.28(2)		
		1	2.38(2)		
	⟨Mn—O⟩		2.13(2)		

number of 6. For example, best-fit parameters obtained for the first coordination shell are summarized in Table 3 for $T = 8.8$ K, 100 K, and 300 K. The mean interatomic distance ⟨Mn—O⟩ was found to be ~2.13 Å that is very close to 2.12 Å [40] expected for the octahedrally coordinated Mn^{2+} and Mn^{3+} ions taken in 1:1 ratio (Fig. 10(a)). So, the local structure around Mn atoms can be described by the sum of two distorted octahedra with different Mn—O distances. The DW factor of the mean Mn—O distance as a function of temperature is plotted in Fig. 10(b). The σ^2 shows a progressive drop below T = 100 K and goes through a minimum near the Neel temperature $T_N = 26$ K. The total variance for DW factor of Mn—O coordination shell is formed by several contributions, with the amplitude of thermal atomic motion and local structure distortions being most important ones. The thermal phonon broadening causes a decrease in σ^2 upon cooling down. Recent specific heat and magnetization measurements have shown the retention of the magnetic short-range correlations up to 100 K, that is, well above T_N [26]. The orbitally non-degenerate Mn^{2+} state ($3d^5$, $S = 5/2$, $L = 0$) was associated with a small uniaxial anisotropy found in Mn_2BO_4. Contrarily, the Mn^{3+} ($3d^4$, $S = L = 2$) is expected to display a strong

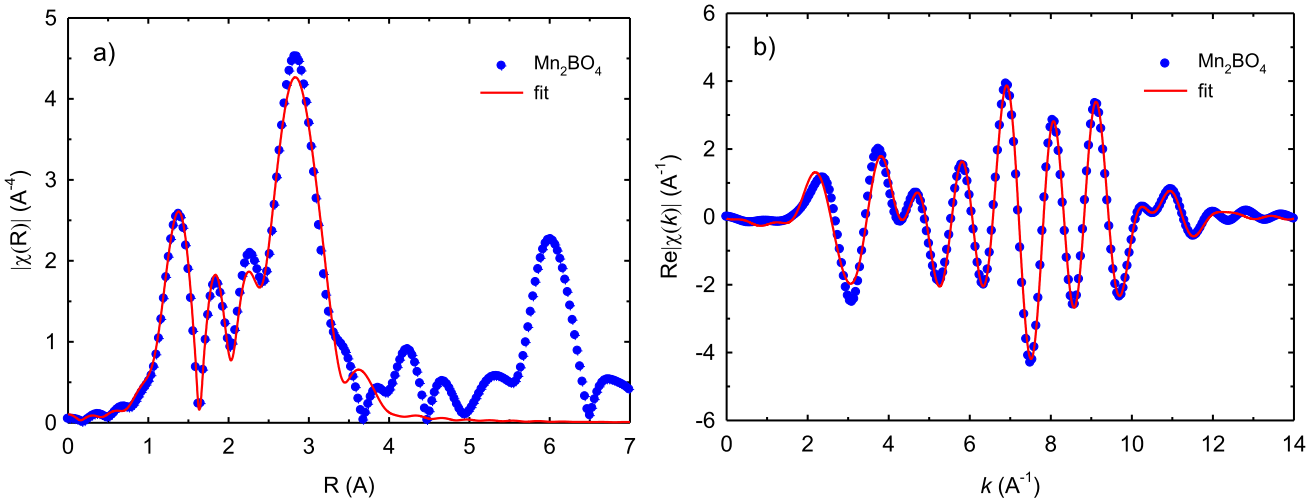

Fig. 9. Comparison between experimental data (blue circles) and best fits (red line) at $T = 8.8$ K. (a) Moduli of the FTs of the $\chi(R)$ EXAFS signals. (b) The real parts of the Fourier-filtered spectra in *k*-space. (For interpretation of the references to color in this figure legend, the reader is referred to the Web version of this article.)

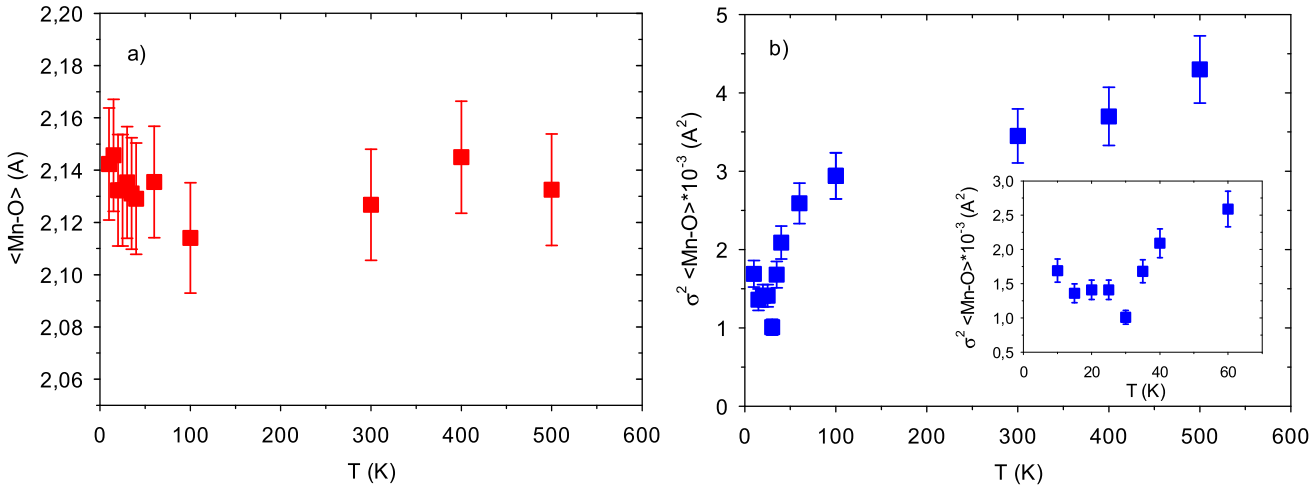

Fig. 10. a) Temperature dependence of the average interatomic distance ⟨Mn−O⟩ in Mn_2BO_4 warwickite; b) DW factors of the ⟨Mn−O⟩ distances as a function of temperature. The inset shows a decrease in the DW factor near to magnetic phase transition T_N = 26 K.

coupling with the lattice due to strong spin-orbital interaction. Thereby, one can suppose that the observed decrease in the DW factor below 100 K is as a result of the decrease of the magnetic correlations through the magnetoelastic interaction.

4. Conclusion

The oxidation states and local structure around Mn ions in mixed-valence warwickite Mn_2BO_4 were studied using the X-ray powder diffraction, X-ray photoelectron and Mn *K*-edge XANES/EXAFS spectroscopies. The measurements were carried out in a wide temperature interval. The crystal structure was refined from XRPD data at 298, 523 and 773 K. The Mn 2*p* photoelectron spectroscopy study as well as XANES measurements confirmed the presence of mixed valence Mn^{2+} and Mn^{3+}. The average manganese oxidation state in bulk was found to be $Mn^{(2.55 \pm 0.08)+}$ appreciably close to nominal $Mn^{2.5+}$ as expected. The DW factor of Mn−O coordination shell was found to progressively reduce below T = 100 K and go through a minimum at the Neel temperature, making Mn_2BO_4 a candidate for applications based on the magnetoelastic interaction. The XRPD data revealed the persistence of monoclinic symmetry up to 973 K. The large bond-valence difference between two Mn sites ($\Delta BVS \approx 1$ v.u.) suggests the presence of Mn^{2+} and Mn^{3+} charge ordering resulted from stacking of the Jahn-Teller distorted MnO_6 octahedra in a double-chain manner that is preferable for the monoclinic structure. The strong pinning of the Mn^{3+} lattice on a crystal lattice is supposed to induce the charge localization and significant electron-lattice effects.

Acknowledgments

This work has been financed by Russian Foundation for Basic Research (17-02-00826 and 16-32-60049 grant numbers).

Appendix A. Supplementary data

Supplementary data to this article can be found online at https://doi.org/10.1016/j.physb.2019.02.019.

References

[1] Y. Tokura, Colossal Magnetoresistive Oxides, CRC Press, London, 2000.
[2] E.J.W. Verwey, Electronic conduction of magnetite (Fe3O4) and its transition point at low temperatures, Nature 144 (3642) (1939) 327–328.
[3] M. Brunner, J.-L. Tholence, L. Puech, S. Haan, J.J. Capponi, R. Calemczuk, J.C. Fernandes, M.A. Continentino, Low-energy excitations in the random magnetic chain system MgTiBO4, Physica B 233 (1) (1997) 37–42.
[4] T.G. Rappoport, L. Ghivelder, J.C. Fernandes, R.B. Guimaraes, M.A. Continentino, Phys. Rev. B 75 (2007) 054422.
[5] A. Arauzo, N.V. Kazak, N.B. Ivanova, M.S. Platunov, Y.V. Knyazev, O.A. Bayukov, L.N. Bezmaternykh, I.S. Lyubutin, K.V. Frolov, S.G. Ovchinnikov, J. Bartolomé, Spin-glass behavior in single crystals of hetero-metallic magnetic warwickites MgFeBO4, Mg0.5Co0.5FeBO4, and CoFeBO4, J. Magn. Magn. Mater. 392 (2015) 114–125.
[6] J.C. Fernandes, R.B. Guimaraes, M.A. Continentino, H.A. Borges, J.V. Valarelli, A. Lacerda, Titanium-III warwickites: a family of one-dimensional disordered magnetic systems, Phys. Rev. B 50 (22) (1994) 16754–16757.
[7] J.P. Attfield, A.M.T. Bell, L.M. Rodriguez-Martinez, J.M. Greneche, R.J. Cernik, J.F. Clarke, D.A. Perkins, Electrostatically driven charge-ordering in Fe2OBO3, Nature 396 (6712) (1998) 655–658.
[8] J.J. Capponi, J. Chenavas, J.C. Joubert, Sur de nouveaux borates mixtes des métaux de transition isotypes de la warwickite, J. Solid State Chem. 7 (1) (1973) 49–54.
[9] N.V. Kazak, A.D. Balaev, N.B. Ivanova, S.G. Ovchinnikov, Mossbauer magnetization and resistivity studies of Fe1.91V0.09BO4, Phys. B Condens. Matter 359–361 (2005) 1324–1326.
[10] A. Apostolov, M. Mikhov, P. Tcholakov, Magnetic properties of boron ferrites FeBMeO4, Phys. Status Solidi A 56 (1) (1979) K33–K36.
[11] M.S. Platunov, N.V. Kazak, Y.V. Knyazev, L.N. Bezmaternykh, E.M. Moshkina, A.L. Trigub, A.A. Veligzhanin, Y.V. Zubavichus, L.A. Solovyov, D.A. Velikanov, S.G. Ovchinnikov, Effect of Fe-substitution on the structure and magnetism of single crystals Mn2-xFexBO4, J. Cryst. Growth 475 (2017) 239–246.
[12] A.D. Balaev, O.A. Bayukov, A.D. Vasil'ev, D.A. Velikanov, N.B. Ivanova, N.V. Kazak, S.G. Ovchinnikov, M. Abd-Elmeguid, V.V. Rudenko, Magnetic and electrical properties of Fe1.91V0.09BO4 warwickite, J. Exp. Theor. Phys. 97 (5) (2003) 989–995.
[13] A. Wiedenmann, P. Burlet, R. Chevalier, Mössbauer study of imperfect one dimensional magnetic systems FeMgBO4 and FeMg2BO5, J. Magn. Magn. Mater. 15–18 (1980) 216–218.
[14] R.B. Guimarães, J.C. Fernandes, M.A. Continentino, H.A. Borges, C.S. Moura, J.B.M. da Cunha, C.A. dos Santos, Dimensional crossover in magnetic warwickites, Phys. Rev. B 56 (1) (1997) 292–299.
[15] I.S. Lyubutin, N.Y. Korotkov, K.V. Frolov, N.V. Kazak, M.S. Platunov, Y.V. Knyazev, L.N. Bezmaternykh, S.G. Ovchinnikov, A. Arauzo, J. Bartolomé, Spin-glass behavior of warwickite MgFeBO4 and CoFeBO4 crystals observed by Mössbauer spectroscopy, J. Alloy. Comp. 642 (2015) 204–209.
[16] J.P. Attfield, J.F. Clarke, D.A. Perkins, Phys. B Condens. Matter 180–181 (1992) 581.
[17] R. Norrestam, M. Kritikos, A. Sjödin, Manganese(II,III) oxyborate, Mn2OBO3: a distorted homometallic warwickite-synthesis, crystal structure, band calculations, and magnetic susceptibility, J. Solid State Chem. 114 (2) (1995) 311–316.
[18] E.M. Carnicom, K. Górnicka, T. Klimczuk, R.J. Cava, The homometallic warwickite V 2 OBO 3, J. Solid State Chem. 265 (2018) 319–325.
[19] A. Akrap, M. Angst, P. Khalifah, D. Mandrus, B.C. Sales, L. Forró, Phys. Rev. B 82 (1–7) (2010) 165106.
[20] M. Angst, P. Khalifah, R.P. Hermann, H.J. Xiang, M.-H. Whangbo, V. Varadarajan, J.W. Brill, B.C. Sales, D. Mandrus Phys, Rev. Lett. 99 (2007) 086403.
[21] S.R. Bland, M. Angst, S. Adiga, V. Scagnoli, R.D. Johnson, J. Herrero-Martín, P.D. Hatton, Phys. Rev. B 82 (2010) 115110.
[22] A.P. Douvalis, V. Papaefthymiou, A. Moukarika, T. Bakas, Hyperfine Interact. 126 (1/4) (2000) 319–327.
[23] G.R. Hearne, W.N. Sibanda, E. Carleschi, V. Pishedda, J.P. Attfield, Phys. Rev. B 86 (2012) 195134.
[24] I. Leonov, A.N. Yaresko, V.N. Antonov, J.P. Attfield, V.I. Anisimov, Phys. Rev. B 72 (2005) 014407.
[25] R.J. Goff, A.J. Williams, J.P. Attfield, Phys. Rev. B 70 (2004) 014426.
[26] N.V. Kazak, M.S. Platunov, Y.V. Knyazev, N.B. Ivanova, O.A. Bayukov,

A.D. Vasiliev, L.N. Bezmaternykh, V.I. Nizhankovskii, S.Y. Gavrilkin, K.V. Lamonova, S.G. Ovchinnikov, Uniaxial anisotropy and low-temperature antiferromagnetism of Mn 2 BO 4 single crystal, J. Magn. Magn Mater. 393 (2015) 316–324.
[27] M. Matos, R.B. Oliveira, One-electron approach to describe charge and orbital order in Mn2OBO3, Int. J. Quantum Chem. 106 (13) (2006) 2737–2746.
[28] H.M. Rietveld, A profile refinement method for nuclear and magnetic structures, J. Appl. Crystallogr. 2 (2) (1969) 65–71.
[29] L.A. Solovyov, Full-profile refinement by derivative difference minimization, J. Appl. Crystallogr. 37 (5) (2004) 743–749.
[30] S.I. Zabinski, J.J. Rehr, A. Ankudinov, R.C. Alber, Phys. Rev. B 52 (1995) 2995.
[31] M. Newville, IFEFFIT: interactive XAFS analysis and FEFF fitting, J. Synchrotron Radiat. 8 (2) (2001) 322–324.
[32] Supplementary materials for: Study of mixed-valence Mn_2BO_4 using XRD, XPS and XAFS spectroscopies.
[33] N.V. Kazak, M.S. Platunov, Y.V. Knyazev, E.M. Moshkina, S.Y. Gavrilkin, O.A. Bayukov, M.V. Gorev, E.I. Pogoreltsev, G.M. Zeer, S.M. Zharkov, S.G. Ovchinnikov, Fe-induced enhancement of antiferromagnetic spin correlations in Mn2 − xFexBO4, J. Magn. Magn Mater. 452 (2018) 90–99.
[34] I.D. Brown, D. Altermatt, Bond-valence parameters obtained from a systematic analysis of the inorganic crystal structure database, Acta Crystallogr. 41 (4) (1985) 244–247.
[35] K. Kumari, S. Ram, R.K. Kotnala, Self-controlled growth of Fe3BO6 crystallites in shape of nanorods from iron-borate glass of small templates, Mater. Chem. Phys. 129 (3) (2011) 1020–1026.
[36] E. Talik, M. Kruczek, A. Pajączkowska, A. Kłos, L. Lipińska, E. Łojko, Chemical analysis of GdCa4O(BO3)3 by XPS method, J. Alloy. Comp. 442 (1–2) (2007) 282–285.
[37] M.C. Biesinger, B.P. Payne, A.P. Grosvenor, L.W.M. Lau, A.R. Gerson, R.S.C. Smart, C. Smart, Resolving surface chemical states in XPS analysis of first row transition metals, oxides and hydroxides: Cr, Mn, Fe, Co and Ni, Appl. Surf. Sci. 257 (7) (2011) 2717–2730.
[38] E.S. Ilton, J.E. Post, P.J. Heaney, F.T. Ling, S.N. Kerisit, XPS determination of Mn oxidation states in Mn (hydr)oxides, Appl. Surf. Sci. 366 (2016) 475–485.
[39] D. Cabaret, C. Brouder, J. Phys. Conf. 190 (2009) 012003.
[40] R.D. Shannon, Revised effective ionic radii and systematic studies of interatomic distances in halides and chalcogenides, Acta Crystallogr. A 32 (5) (1976) 751–767.